



Rational design of hierarchically porous birnessite-type manganese dioxides nanosheets on different one-dimensional titania-based nanowires for high performance supercapacitors

Yu Xin Zhang ^{a, b, *}, Min Kuang ^a, Xiao Dong Hao ^a, Yan Liu ^{c, d, **}, Ming Huang ^a, Xiao Long Guo ^a, Jing Yan ^{c, d}, Gen Quan Han ^{c, d}, Jing Li ^e

^a College of Materials Science and Engineering, Chongqing University, Chongqing 400044, PR China

^b National Key Laboratory of Fundamental Science of Micro/Nano-Devices and System Technology, Chongqing University, Chongqing 400044, PR China

^c Key Laboratory of Optoelectronic Technology and Systems of the Education Ministry, Chongqing University, Chongqing 400044, PR China

^d College of Optoelectronic Engineering, Chongqing University, Chongqing 400044, PR China

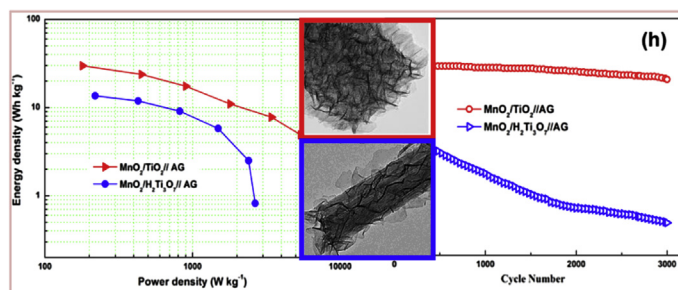
^e Department of Chemistry, Tongji University, Shanghai 200092, PR China



HIGHLIGHTS

- MnO₂ nanosheets were decorated on 1D TiO₂ nanowires by a facile and large-scale method.
- The MnO₂/TiO₂ core–shell architecture exhibited a high capacitance of 120 F g⁻¹ (0.1 A g⁻¹).
- Excellent cycling stability: 93% capacitance retention after 3000 cycles.
- The asymmetric supercapacitor yielded a maximum energy density of 29.8 Wh kg⁻¹.

GRAPHICAL ABSTRACT



ARTICLE INFO

Article history:

Received 27 April 2014

Received in revised form

8 July 2014

Accepted 17 July 2014

Available online 25 July 2014

Keywords:

Manganese oxides

Titania

Supercapacitors

Nanocomposites

ABSTRACT

A facile and large-scale strategy of mesoporous birnessite-type manganese dioxide (MnO₂) nanosheets on one-dimension (1D) H₂Ti₃O₇ and anatase/TiO₂ (B) nanowires (NWs) is developed for high performance supercapacitors. The morphological characteristics of MnO₂ nanoflakes on H₂Ti₃O₇ and anatase/TiO₂ (B) NWs could be rationally designed with various characteristics (e.g., the sheet thickness, surface area). Interestingly, the MnO₂/TiO₂ NWs exhibit a more optimized electrochemical performance with specific capacitance of 120 F g⁻¹ at current density of 0.1 A g⁻¹ (based on MnO₂ + TiO₂) than MnO₂/H₂Ti₃O₇ NWs. An asymmetric supercapacitor of MnO₂/TiO₂//activated graphene (AG) yields a better energy density of 29.8 Wh kg⁻¹ than MnO₂/H₂Ti₃O₇//AG asymmetric supercapacitor, while maintaining desirable cycling stability. Indeed, the pseudocapacitive difference is related to the substrates, unique structure and surface area. Especially, the anatase/TiO₂ (B) mixed-phase system can provide good electronic conductivity and high utilization of MnO₂ nanosheets.

© 2014 Elsevier B.V. All rights reserved.

* Corresponding author. College of Materials Science and Engineering, Chongqing University, Chongqing 400044, PR China. Tel./fax: +86 23 65104131.

** Corresponding author. College of Optoelectronic Engineering, Chongqing University, Chongqing 400044, PR China.

E-mail addresses: zhangyuxin@cqu.edu.cn (Y.X. Zhang), [\(Y. Liu\).](mailto:cqliuyan@cqu.edu.cn)

1. Introduction

Supercapacitors, owing to low cost, high power density, small size, rapid charging/discharging rates and long cycle life, are considered to be a kind of important energy conversion and storage

device [1–3]. According to charge storage mechanisms, supercapacitors can be classified into two types [4,5]: (I) Electrochemical double layer capacitors (EDLCs) are based on surface reaction at the electrode materials/electrolyte interface. Various carbon materials with high surface area such as carbon aerogels, grapheme and mesoporous carbons have been used as electrode materials or substrates for supercapacitors [6–8]. (II) Pseudocapacitors are based on Faradaic redox reactions occurring at the electrode materials surface. Transition-metal oxides (NiO, RuO₂, MnO₂, Co₃O₄, TiO₂ and ZnO) [9–13] and conducting polymers [14,15] generally display pseudocapacitive behavior. Potentially, the pseudocapacitors have much higher capacitance compared with the EDLCs [9–13].

Much effort has been devoted to improve the device energy and power densities of transition metal oxides owing to their easy availability as well as comparable electrochemical behavior [16], variable oxidation states and multi-electron transfer during the faradaic reactions [17]. In comparison to other transition metal oxides, manganese oxide-based supercapacitors are considered as alternative device for supercapacitors owing to their environmental friendliness, wide potential window, good electrochemical performance, natural abundance and low cost [18–20]. The charge storage mechanism for MnO₂ is widely accepted to be based on redox reactions, including (1) the surface adsorption of electrolyte cations; (2) the intercalation/de-intercalation of alkali cations in the bulk [6,21]. However, the densely packed structure, low surface area and poor electronic conductivity of MnO₂ severely limit practical capacitance [22–24]. Thus, various manganese oxide-based supercapacitors are developed to enhance electrical conductivity, morphological properties, porosity and surface area etc. [25] by introducing difference substrates, which can significantly affect electro activities and structural features of MnO₂ leading to high charge/discharge capacities and short diffusion paths for ion and electron transport which may improve the utilization of MnO₂ materials.

Among various substrates, one-dimensional (1D) inorganic nanostructured materials (nanowires and nanotubes arrays) have garnered sustained research interest owing to their promising charge transport ability, compared to traditional materials [26,27]. Among those 1D inorganic nanomaterials, titanic oxide-based nanowires seem to be extremely attractive for hybrid-supercapacitor applications because of their high chemical/thermal stability, suppression of structural distortion [28], enhanced cycling stability and improved reversibility [29,30], and more active sites for ions and electron to deliver a higher energy-density [31,32]. Moreover, the titanic oxide-based nanowires have higher electrical conductivity ($10^{-5} \sim 10^{-2} \text{ S cm}^{-1}$) than MnO₂ ($10^{-6} \sim 10^{-5} \text{ S cm}^{-1}$) [28]. In addition, it has been reported that, one-dimensional single-crystalline nanostructures are superior to polycrystalline counterparts in electron transport [33,34].

In this work, well-designed MnO₂-based nanostructured electrodes with two different 1D nanowires: (1) H₂Ti₃O₇ and (2) anatase/TiO₂ (B) are synthesized via an one-step hydrothermal method without carbon coating. The morphology, structure and electrochemical properties of the composites electrodes are examined. Moreover, the electrochemical properties of the asymmetric supercapacitors of MnO₂/TiO₂/AG and MnO₂/H₂Ti₃O₇/AG are investigated for comparison.

2. Experimental section

2.1. Synthesis of H₂Ti₃O₇ and TiO₂ NWs

All reagents were of analytical purity and used without any further purification. Synthesis of H₂Ti₃O₇ nanowires was

performed via a hydrothermal process. In a typical synthesis, commercial anatase TiO₂ powders (0.4 g) were put into aqueous solution of 10 M NaOH (35 mL) in a Teflon-lined stainless steel autoclave (50 mL). The autoclave was kept at 180 °C for 48 h. After hydrothermal treatment, the resulting precipitates were acid-washed (0.1 M HCl solution) to realize the full-ion exchange from Na⁺ to H⁺. The final white products were then dried in vacuum at 80 °C for 8 h, and then calcined at 400 °C for 3 h in air to obtain the anatase/TiO₂ (B) nanowires.

2.2. Synthesis of the MnO₂ nanosheets on H₂Ti₃O₇ and TiO₂ NWs

In a typically synthesis, 25 mg H₂Ti₃O₇ (or TiO₂) were dispersed in KMnO₄ solution (40 mL, 0.01 M) by ultrasonication for 10 min. The mixed solution was then transferred into a Teflon-lined stainless steel autoclave with a capacity of 50 mL. The autoclave was directly put in an electric oven at 140 °C for 24 h and then cooled to room temperature. The black resultants were collected by centrifugation and dried at 60 °C for 12 h in a vacuum oven.

2.3. Materials characterization

The structure and morphology investigations of the samples were carried out with focused ion beam scanning electron microscopy (ZEISS AURIGA FIB/SEM) and transmission electron microscopy (TEM, ZEISS LIBRA 200). The chemical composition and crystallographic information of as-prepared products were established by powder X-ray diffraction (XRD, D/max 1200, Cu K α). Nitrogen adsorption–desorption isotherms were obtained using a micromeritics ASAP 2020 sorptometer to assess surface area and porosity.

2.4. Electrochemical measurements

All the electrochemical tests were conducted with an electrochemical workstation (CHI 660E) using a conventional three electrode system where a mixture of active materials, carbon black, and polyvinylidene fluoride (PVDF) (7:2:1 wt.%), a Ag/AgCl and a platinum plate were used as working, reference electrodes and counter, respectively. The positive electrodes were investigated by cyclic voltammetry (CV) technique with varying the potential between 0 and 0.8 V at a rate ranged from 5 to 50 mV s⁻¹. Galvanostatic charge–discharge (GCD) experiments were performed with current densities of 0.1–10 A g⁻¹ at a potential of 0–0.7 V. The electrochemical impedance spectroscopy (EIS) was conducted in the frequency range between 100 kHz and 0.01 Hz with a perturbation amplitude of 5 mV versus the open-circuit potential.

The electrochemical performance of asymmetric supercapacitor was measured with a two-electrode system including two slices of electrode material with the same size which were assembled together with filter paper soaked in 1 M Na₂SO₄ solution before being connected to the potentiostat. The MnO₂/TiO₂ or MnO₂/H₂Ti₃O₇ NWs were the positive electrode and activated graphenes (AG) were the negative electrode, respectively. CVs were recorded as scan rates of 5, 10, 20, 50, and 80 mV s⁻¹. GCD curves were obtained at constant current densities of 0.2, 0.5, 1, 2, 4 and 6 A g⁻¹. All the operating current densities were calculated based on the total weight of MnO₂/TiO₂ or MnO₂/H₂Ti₃O₇ NWs with AG.

3. Results and discussion

3.1. Structure and morphology

Fig. 1 shows the XRD patterns of H₂Ti₃O₇ NWs and MnO₂/H₂Ti₃O₇ NWs. Almost all the identified peaks can be perfectly

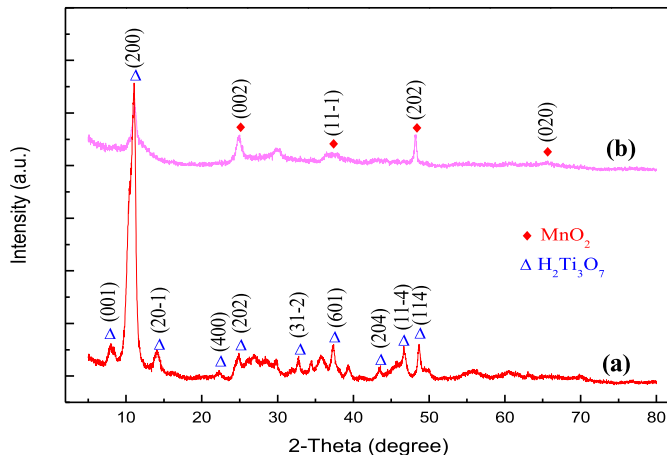


Fig. 1. XRD patterns of pure $\text{H}_2\text{Ti}_3\text{O}_7$ NWs (a) and $\text{MnO}_2/\text{H}_2\text{Ti}_3\text{O}_7$ NWs (b).

indexed to $\text{H}_2\text{Ti}_3\text{O}_7$ (JCPDS NO. 41-0192) and monoclinic potassium birnessite MnO_2 (JCPDS NO. 86-0666). The sharp and strong peaks for as-prepared $\text{H}_2\text{Ti}_3\text{O}_7$ attest the good crystallinity and high purity. After MnO_2 decoration (Fig. 1b), the diffraction peak from the birnessite-type MnO_2 phase is weak, indicating a low mass loading of MnO_2 .

TEM images (Fig. 2a) exhibit that MnO_2 nanosheets-coated $\text{H}_2\text{Ti}_3\text{O}_7$ NWs have uniform diameter (about 80 nm), slightly

larger than pristine $\text{H}_2\text{Ti}_3\text{O}_7$ NWs (ca. 60 nm; see [Supplementary information, SI-1](#)). These as-formed MnO_2 nanosheets with a diameter of 5–10 nm are intercrossed with each other, which create loose porous nanostructures with abundant open space and electroactive surface sites (Fig. 2b). Interestingly, increasing the reaction time to 30 h, the MnO_2 nanoflakes grow larger and the diameters increase to ~20 nm ([SI-2](#)). A high-resolution TEM image (Fig. 2c and d) taken from the zones of the $\text{MnO}_2/\text{H}_2\text{Ti}_3\text{O}_7$ NWs (indicated in Fig. 2b) illustrates that the well-resolved lattice fringe gives an interplanar spacing of 0.36 nm, which is well consistent with the distance of the (110) plane of $\text{H}_2\text{Ti}_3\text{O}_7$ (Fig. 2d). Meanwhile, the interplanar spacing of MnO_2 nanoflake is 0.71 nm (Fig. 2c), which is the typical interplanar spacing of birnessite-type MnO_2 as reported in other literature [35,36]. The selected area electron diffraction (SAED) pattern demonstrates that the $\text{H}_2\text{Ti}_3\text{O}_7$ NWs are monocrystalline (inset in Fig. 2c). The inset in Fig. 2d presents the SAED pattern of the hybrid, and the two diffraction rings are corresponding to the (002) and (113) crystal planes of MnO_2 .

Fig. 3 shows the XRD pattern of TiO_2 NWs and $\text{MnO}_2/\text{TiO}_2$ NWs. Diffractions from the anatase phase (JPCDS 21-1272) and TiO_2 (B) phase (JPCDS 35-0088) are observed after calcination at 400 °C (Fig. 3a), indicating that these nanowires are of mixed anatase and TiO_2 (B) phase. The peaks associated with TiO_2 (B) are more prominent than that of anatase, indicative of better crystallinity of TiO_2 (B). As for the $\text{MnO}_2/\text{TiO}_2$ NWs (Fig. 3b), diffraction peaks from the birnessite-type MnO_2 phase can be observed and the diffraction intensity of the peaks from the TiO_2 phase decreases evidently, indicating a high mass loading of MnO_2 .

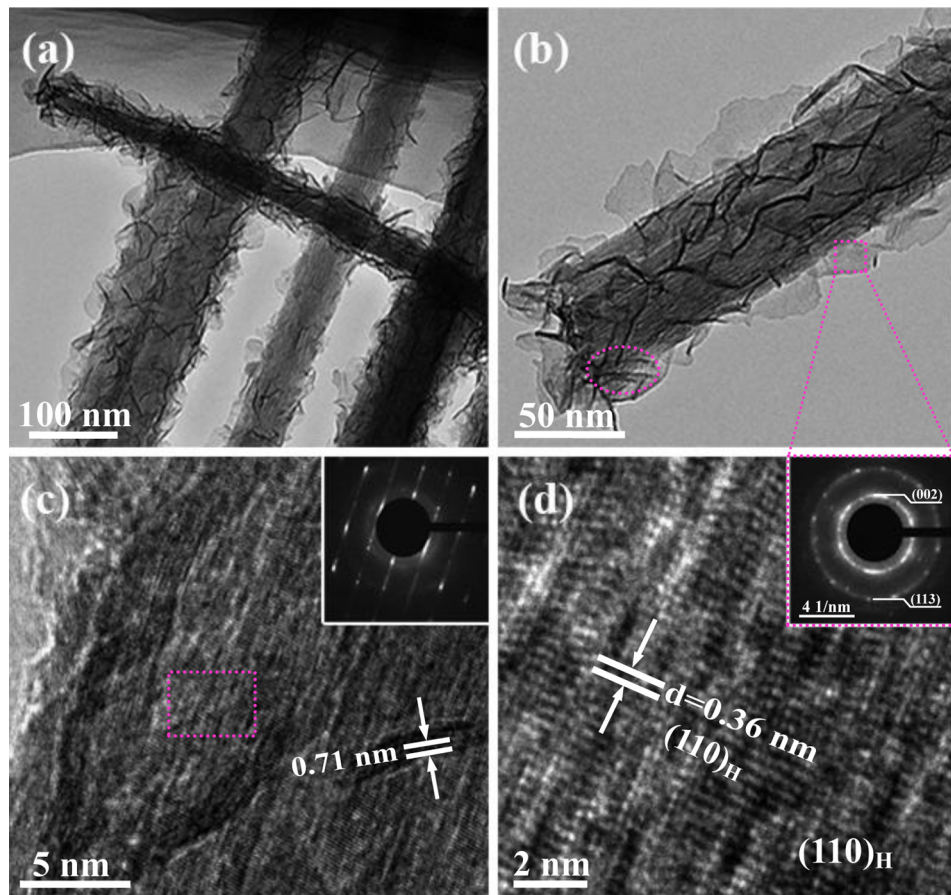


Fig. 2. (a) Low- and (b) high-magnification TEM images of the $\text{MnO}_2/\text{H}_2\text{Ti}_3\text{O}_7$ NWs, (c, d) HRTEM images of the $\text{MnO}_2/\text{H}_2\text{Ti}_3\text{O}_7$ NWs. The insert of (c) and (d) are the SAED patterns from the $\text{MnO}_2/\text{H}_2\text{Ti}_3\text{O}_7$ NWs and MnO_2 nanoflakes respectively.

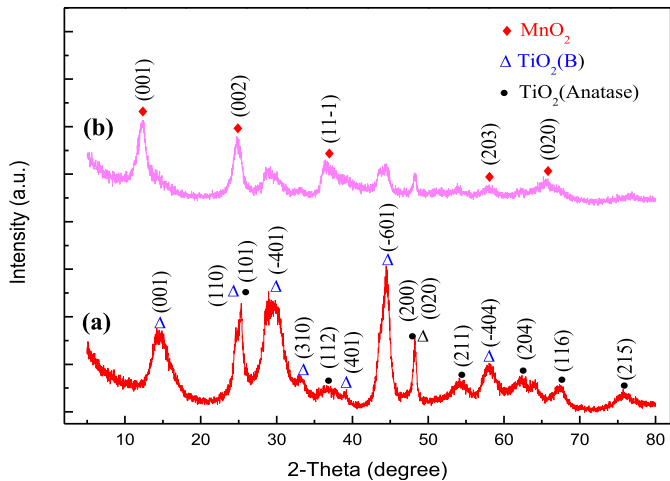


Fig. 3. XRD patterns of anatase/TiO₂ (B) NWs (a) and MnO₂/TiO₂ NWs (b).

The low-magnification SEM and TEM images (SI-1) clearly show an individual TiO₂ NWs with diameter of about 80 nm and lengths of several hundred nanometers. Apparently, after oxidative conversion into mixed phase anatase-TiO₂ (B), the basic morphology of the sample is perfectly conserved without calcination-induced significant alterations. After MnO₂ decoration, the surface of TiO₂ is homogeneously covered with a layer of dense MnO₂ ultrathin nanoflakes (Fig. 4a). The interconnected MnO₂ nanosheets create a highly porous surface morphology. This configuration can provide

an especially high surface area and more active sites for the adsorption of Na⁺, which hence endows the MnO₂ with a very high specific capacitance.

The energy-dispersive X-ray spectroscopy (EDX) (see Supplementary information, SI-3) shows clear evidence of core/shell linear structure with the Mn signal peaks at the outside (shell) of the composite and the Ti signal peak at the inner part (core) of the wire. The interface between MnO₂ and TiO₂ can be distinguished from the gray scale contrast across the nanowire (Fig. 4b), and the nanoflake with diameters of about 30 nm can be clearly observed. Higher-magnification TEM images (Fig. 2c and d) reveal that the interplanar spacing of MnO₂ nanoflake is 0.71 nm, indicative of birnessite-type MnO₂ nanoflakes. The SAED pattern (inset of Fig. 4c) reveals the single-crystalline nature of TiO₂ NWs and the polycrystalline nature of MnO₂. The HRTEM image (Fig. 2d) reveals two sets of lattice fringes with interplane spacings of 0.32 and 0.27 nm, corresponding to the (002) and (310) planes of anatase and TiO₂ (B) phase, respectively.

The nitrogen adsorption and desorption isotherms of the MnO₂/H₂Ti₃O₇ and MnO₂/TiO₂ NWs are shown in Fig. 5. The N₂ adsorption–desorption isotherm is characteristic of type IV with a type H3 hysteresis loop observed in the range 0.7–1.0 P/P₀ (Fig. 5a and b) [3], which suggests the presence of a mesoporous structure for the MnO₂/H₂Ti₃O₇ and MnO₂/TiO₂ NWs [37,38]. The Brunauer–Emmett–Teller (BET) surface area value of the MnO₂/H₂Ti₃O₇ and MnO₂/TiO₂ NWs is calculated to be 39.8 and 57.8 m² g⁻¹, respectively, which is higher than the pristine H₂Ti₃O₇ and TiO₂ NWs (see Supplementary information, SI-4). The pore size distribution of the sample calculated by desorption isotherm using

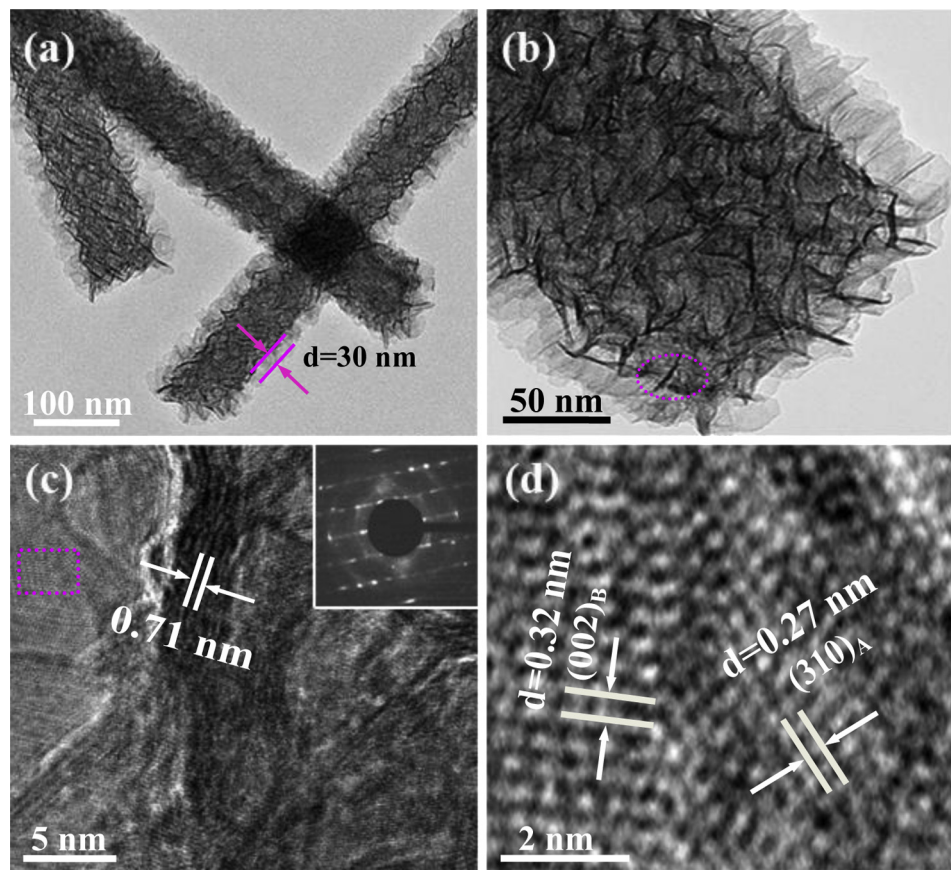


Fig. 4. (a) Low- and (b) high-magnification TEM images of the MnO₂/TiO₂ NWs; (c, d) HRTEM images of the MnO₂/TiO₂ NWs. The insert of (c) is the SAED patterns from the region marked with a rectangle in (b).

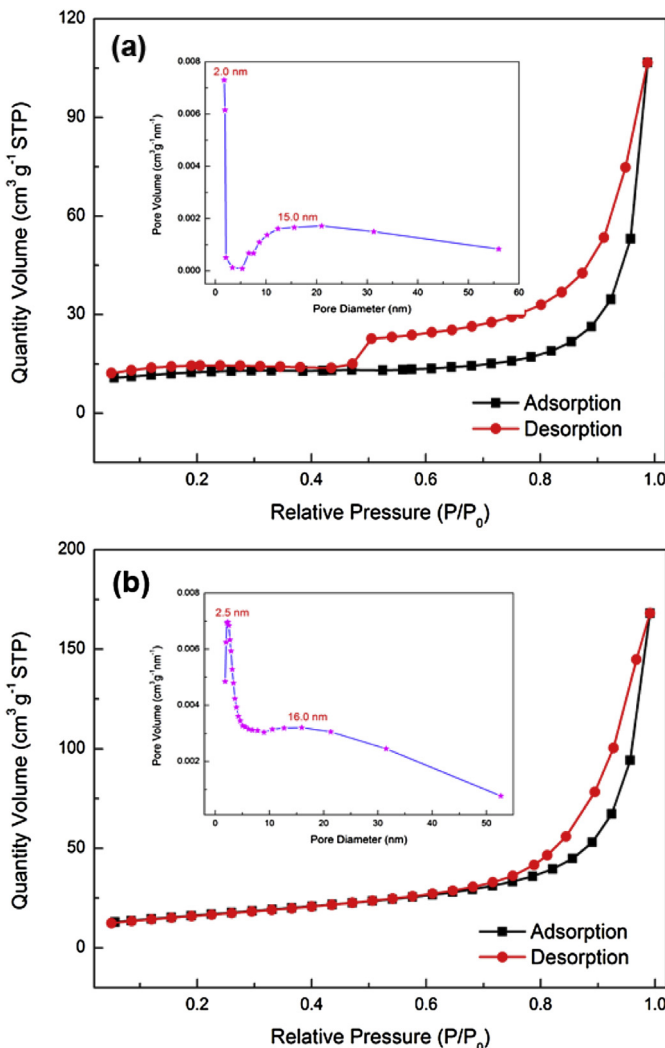


Fig. 5. Nitrogen adsorption and desorption isotherms for the MnO₂/H₂Ti₃O₇ NWs (a), and MnO₂/TiO₂ NWs (b). The insets show the corresponding BJH pore size distributions.

Barret–Joyner–Halenda (BJH) method is shown in inset of Fig. 5. The MnO₂/H₂Ti₃O₇ NWs show a narrow pore size distribution centered at around 1.5 nm, while the MnO₂/TiO₂ NWs have sharp peak at ~2.5 nm. The pore volume of MnO₂/H₂Ti₃O₇ NWs is

calculated as 0.158 cm³ g⁻¹, while the pore volume of MnO₂/TiO₂ NWs is up to 0.261 cm³ g⁻¹. Inconsideration of high surface area and large pore volume, it is expected that the MnO₂/TiO₂ NWs will have impressive electrochemical performance, and further electrochemical measurements have been carried out to prove this hypothesis.

On the basis of observations above, the mass loading of MnO₂ nanoflakes in H₂Ti₃O₇ and TiO₂ NWs is very different, as illustrated in Fig. 6a. H₂Ti₃O₇ is annealed in air at 400 °C for 2 h; the surface of TiO₂ NWs becomes highly porous and active. In addition, FTIR spectra are examined to uncover the surface characteristics of nanowires (Fig. 6b). The basic crystal structure units of H₂Ti₃O₇ NWs are [Ti₃O₇]²⁻ sheets, which will stop [MnO₄]⁻ approaching nanowires due to electrostatic repulsion, while the abundant hydroxyl of TiO₂ NWs speed up the oxidation. It is assumed that surface properties of diverse nanowires would also lead to different deposition density of MnO₂ nanosheets as well as the calcinations and processing time. Additionally, the chemical composition of MnO₂/TiO₂ and MnO₂/H₂Ti₃O₇ are calculated by etching the MnO₂ in HCl solution (37 wt.%) (see *Supplementary information*, Table S1). The MnO₂/TiO₂ mass ratio is 36/64 while the MnO₂/H₂Ti₃O₇ mass ratio is 22/78. It is apparent that MnO₂/TiO₂ NWs has higher mass ratio of MnO₂ compared with MnO₂/H₂Ti₃O₇ NWs under similar feed mass ratio of Ti-based NWs/KMnO₄ and reaction condition, suggesting that the surface of TiO₂ NWs contributes to the growth of MnO₂ nanosheets.

Herein, a general growth mechanism for the unique MnO₂/TiO₂ NWs is proposed, on the basis of above analysis and SI-5. When the mixed solution of TiO₂ and KMnO₄ solution is treated under hydrothermal condition for 4 h, the TiO₂ NWs surfaces become rough, initially decorated by many tiny MnO₂ “buds” which are produced by the decomposition of KMnO₄. With the reaction time increases to 8 h, the rudiments of MnO₂ nanosheets are formed, and then fully develop when the reaction time is prolonged to 24 h. Moreover, increasing the reaction time to 30 h, the MnO₂ nanosheets grow larger and the morphologies of bending, curling, and crumpling are clearly observed (SI-5 and SI-6).

3.2. Electrochemical performances

The transportation of electrolytes through the MnO₂/TiO₂-based nanostructures is feasible for efficient redox reactions during Faradaic charge storage process because of their hierarchical structure. However, the charge storage efficiency of these structures may vary because of their observed differences (e.g., the morphology and size). To evaluate their electrochemical

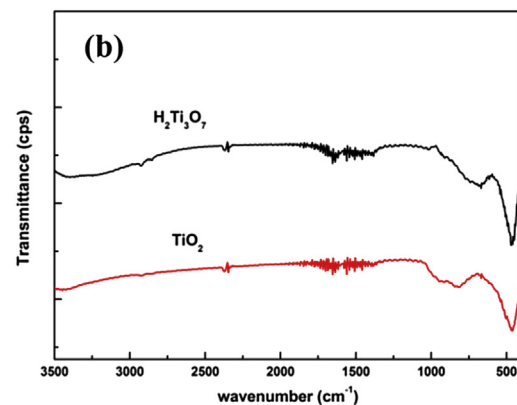
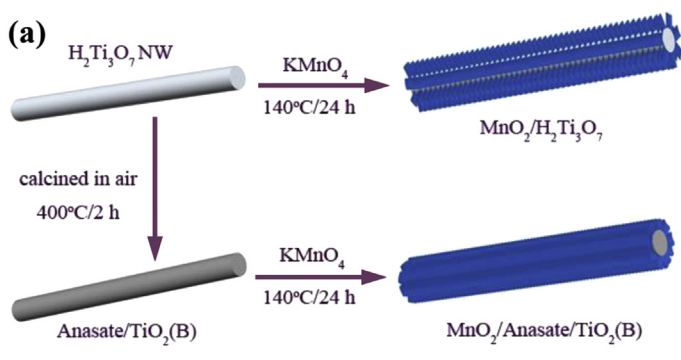


Fig. 6. (a) Schematic diagram illustrating the processes for growth MnO₂ nanoflakes on H₂Ti₃O₇ and anasate/TiO₂ (B) NWs; (b) FTIR of pristine H₂Ti₃O₇ and TiO₂ NWs.

performance, cyclic voltammetry (CV) and galvanostatic charge–discharge measurements are performed. Representative CV curves for the $\text{MnO}_2/\text{TiO}_2$ and $\text{MnO}_2/\text{H}_2\text{Ti}_3\text{O}_7$ NWs in three electrode configuration at different scan rates are shown in Fig. 7a and b. Both $\text{MnO}_2/\text{H}_2\text{Ti}_3\text{O}_7$ and $\text{MnO}_2/\text{TiO}_2$ NWs exhibit ideal rectangular and symmetric CV curves at low scanning rates (5 and 10 mV s^{-1}), proving the ideal pseudo-capacitive nature with fast charge–discharge process [39]. Furthermore, the CV profile of $\text{MnO}_2/\text{H}_2\text{Ti}_3\text{O}_7$ NWs deviates seriously from rectangularity and transforms into spindle shape with increasing scanning rates, especially at a high scan rate of 50 mV s^{-1} . This can be ascribed to poor electrical conductivity of $\text{MnO}_2/\text{H}_2\text{Ti}_3\text{O}_7$ NWs and the change of ion transplant surrounding, for which the ions can only reach the

outer surface of the electrode and cannot enter into the interior pores at a large scan rate [17,40]. In contrast, $\text{MnO}_2/\text{TiO}_2$ NWs present close-rectangular CV curves over in wide range of scanning rates (5–50 mV s^{-1}). This is because $\text{MnO}_2/\text{TiO}_2$ NWs nanostructures have relatively appropriate pore size and surface texture. Furthermore, the existence of TiO_2 facilitates charge transfer to the MnO_2 phase. The area of $\text{MnO}_2/\text{TiO}_2$ NWs under the CV curve is clearly much larger than that of $\text{MnO}_2/\text{H}_2\text{Ti}_3\text{O}_7$ NWs at the same scan rate, suggesting a high specific capacitance and utilization of MnO_2 in the hybrids.

The galvanostatic charge/discharge (GCD) tests of the $\text{MnO}_2/\text{TiO}_2$ and $\text{MnO}_2/\text{H}_2\text{Ti}_3\text{O}_7$ NWs at different constant current densities (Fig. 6c and d) present that the curve of $\text{MnO}_2/\text{TiO}_2$ NWs is linear and

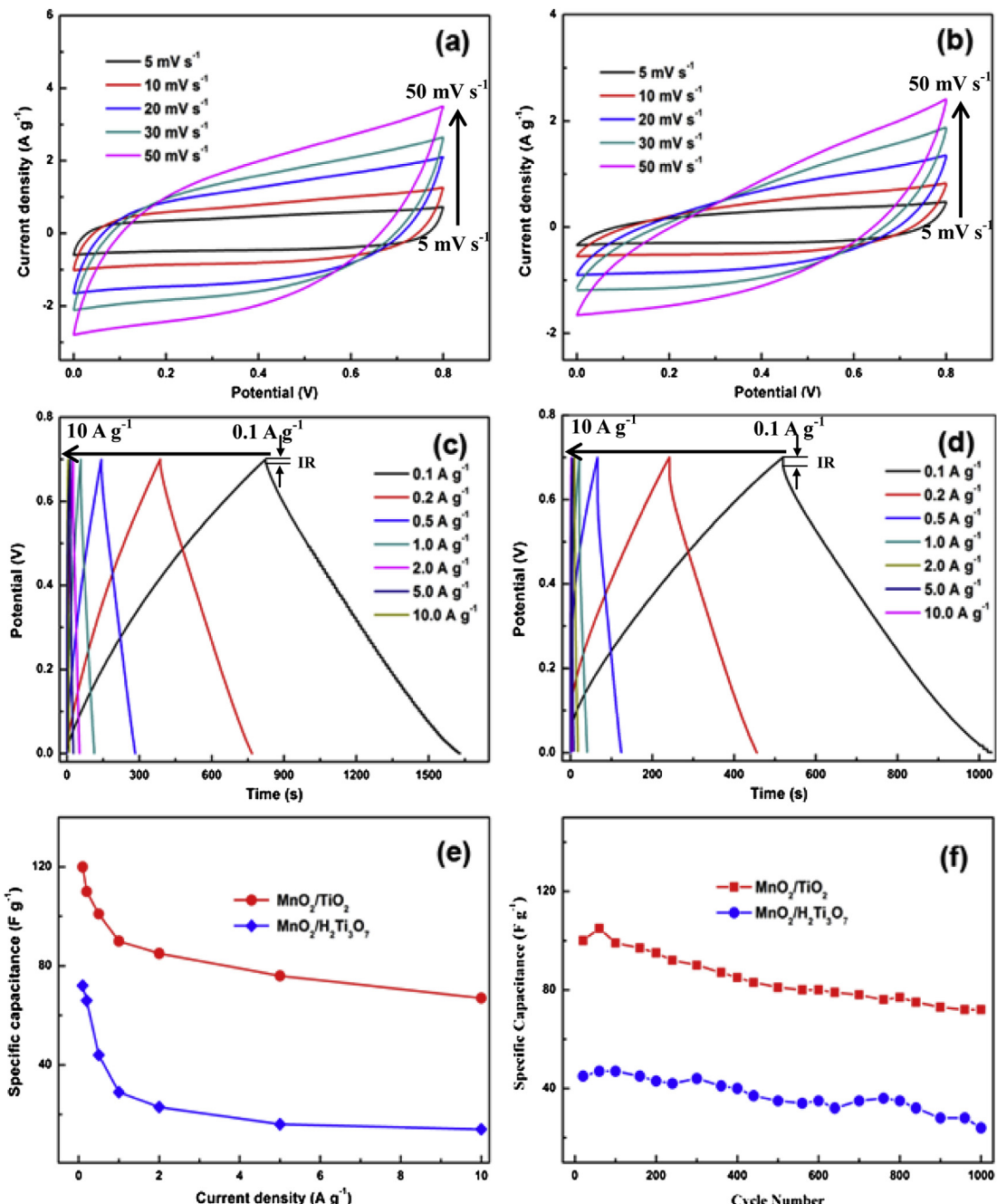


Fig. 7. (a, b) CV curves, (c, d) charge–discharge curves, (e) capacitances versus current densities, and (f) variation of capacitance with cycle number at 0.3 A g^{-1} of the (a, b) $\text{MnO}_2/\text{TiO}_2$ NWs and the (c, d) $\text{MnO}_2/\text{H}_2\text{Ti}_3\text{O}_7$ NWs.

symmetric, indicating an ideal capacitor, capable of reversible charging and discharging [41]. In comparison, the curve of $\text{MnO}_2/\text{H}_2\text{Ti}_3\text{O}_7$ NWs is distorted to some extent. Furthermore, the IR drop (marked in Fig. 6c and d) of $\text{MnO}_2/\text{TiO}_2$ NWs is much lower than that of $\text{MnO}_2/\text{H}_2\text{Ti}_3\text{O}_7$ NWs, indicating that the introduction of TiO_2 reduces significantly internal resistance. Low internal resistance is very favorable in energy storage devices, which reduces energy waste during charging/discharging processes. The increase in the charging time represents the higher capacitance of the $\text{MnO}_2/\text{TiO}_2$ NWs. According to the GCD curves, the specific capacitances of the electrodes are respectively calculated using the following equation [42]:

$$C_m = \frac{I\Delta t}{m\Delta V}$$

where m , I , Δt and ΔV are the weight (g) of the electroactive materials, discharge current (A), the discharging time (s), and the discharging potential range (V), respectively. The specific capacitance of $\text{MnO}_2/\text{TiO}_2$ and $\text{MnO}_2/\text{H}_2\text{Ti}_3\text{O}_7$ NWs obtained from the discharging curves are calculated to be 120 F g^{-1} and 72 F g^{-1} at the current density of 0.1 A g^{-1} , respectively. It is due to that the highly porous structure and high specific surface area of the TiO_2 shell facilitate the ions to transfer into the porous structure more easily which would lead to substantial redox faradic reactions and surface adsorption of electrolyte cations. Maximizing the utilization of MnO_2 is always considered as a challenge because only the surface of oxides can be utilized for charge storage. Herein, the comparison of the specific capacitance (based on the mass of MnO_2 alone) between this work and previous reports is summarized (Table S2). The normalized specific capacitance of $\text{MnO}_2/\text{TiO}_2$ NWs in this work is 334 F g^{-1} at the current density of 0.1 A g^{-1} , much higher than that of MnO_2 -activated carbon electrode (228 F g^{-1}) [43], MnO_2 -graphene composites electrode (234.2 F g^{-1}) [44], RGO/ MnO_2 electrode (260 F g^{-1}) [45], and graphene/ MnO_2 /polyaniline electrode (276 F g^{-1}) [36].

The rate capability of $\text{MnO}_2/\text{TiO}_2$ and $\text{MnO}_2/\text{H}_2\text{Ti}_3\text{O}_7$ NWs is also evaluated by charging–discharging at different current densities (Fig. 7e). The $\text{MnO}_2/\text{TiO}_2$ NWs maintain their 58.9% capacitance as the current density is increased from 0.1 to 10 A g^{-1} , while the $\text{MnO}_2/\text{H}_2\text{Ti}_3\text{O}_7$ NWs lose 80.6% of their capacity in the same condition, indicating that the $\text{MnO}_2/\text{TiO}_2$ NWs have better rate capability, in good accordance with the CV tests. Additionally, the specific capacitance based on MnO_2 mass alone versus current density is addressed in Table S3.

The cycling stability of $\text{MnO}_2/\text{TiO}_2$ and $\text{MnO}_2/\text{H}_2\text{Ti}_3\text{O}_7$ NWs in $1 \text{ M Na}_2\text{SO}_4$ electrolyte at a current density of 1 A g^{-1} is shown in Fig. 7f. The specific capacitance of $\text{MnO}_2/\text{TiO}_2$ NWs increases in the initial 60 cycles owing to the improved wetting by applying a potential, and then only a little fading can be observed and the capacitance retention is 95% after 1000 cycles. As for the $\text{MnO}_2/\text{H}_2\text{Ti}_3\text{O}_7$ NWs the decay in specific capacitance after a 1000-cycle test is 40%. These results also indicate that the $\text{MnO}_2/\text{TiO}_2$ NWs have a better cycling performance, in comparison with the $\text{MnO}_2/\text{H}_2\text{Ti}_3\text{O}_7$ NWs.

The EIS analysis has been recognized as one of the principal methods for examining the fundamental behavior of electrode materials, which not only provides useful information on the electrochemical frequency of the system but also allows for the measurement of redox reaction resistance and equivalent series resistance of the electrode [40]. As presented in Fig. 8, the Nyquist plots can be divided into two parts: one semicircle in the high-frequency, and a straight line inclining about 45° to the real axis or an almost vertical line in the low frequency region [46–48]. At the high frequencies, semicircles can be observed with the diameters representing the charge-transfer resistance (R_{ct}) [46]. It is apparent that $\text{MnO}_2/\text{TiO}_2$ NWs have a much smaller R_{ct} than $\text{MnO}_2/\text{H}_2\text{Ti}_3\text{O}_7$ NWs.

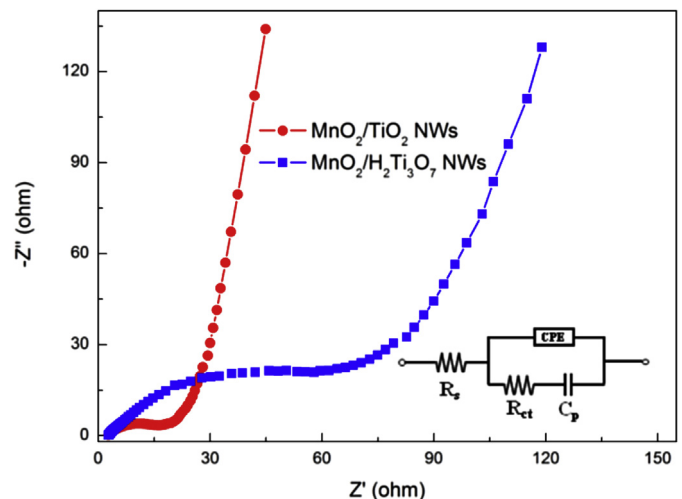


Fig. 8. Nyquist plots for $\text{MnO}_2/\text{TiO}_2$ and $\text{MnO}_2/\text{H}_2\text{Ti}_3\text{O}_7$ NWs in the frequency range of 100 kHz – 0.01 Hz . Insert shows the equivalent circuit for the electrochemical impedance spectrum.

$\text{H}_2\text{Ti}_3\text{O}_7$ NWs. The slope of 45° portion in the transitory frequency next to the semicircle and the noticeable linear part at the low frequency region of the respective Nyquist plots is called Warburg resistance (W) [49], which originates from the frequency dependence of ion diffusion/transport from the electrolyte to the electrode surface [50,51]. As shown in the Fig. 8, $\text{MnO}_2/\text{TiO}_2$ NWs electrode has a smaller Warburg region, presenting a minor Warburg resistance. It implies that the highly porous $\text{MnO}_2/\text{TiO}_2$ NWs are able to facilitate the penetration of electrolyte, leading to fast diffusion of electrolyte into the pores of MnO_2 . It can be seen that the slope of the straight line for the $\text{MnO}_2/\text{TiO}_2$ NWs is much larger than that of the $\text{MnO}_2/\text{H}_2\text{Ti}_3\text{O}_7$ NWs. This observation indicates that the $\text{MnO}_2/\text{TiO}_2$ NWs have much lower diffusive resistance than the $\text{MnO}_2/\text{H}_2\text{Ti}_3\text{O}_7$ NWs. After cycling for 1000 times (SI-7), the R_s of $\text{MnO}_2/\text{TiO}_2$ and $\text{MnO}_2/\text{H}_2\text{Ti}_3\text{O}_7$ NWs increase from 1.5 and 1.8Ω to 2.6 and 2.9Ω , respectively. EIS analytical results further verify that $\text{MnO}_2/\text{TiO}_2$ NWs exhibits good cycling stability compared with $\text{MnO}_2/\text{H}_2\text{Ti}_3\text{O}_7$ NWs, which is attributed to the following factors: (1) the conductive electronic and ion transport capability of unique architecture of anatase/ TiO_2 (B) mixed-phase system is higher than that of $\text{H}_2\text{Ti}_3\text{O}_7$ NWs, which is due to the heterojunction of anatase/ TiO_2 (B) mixed-phase. (2) The pristine anatase/ TiO_2 (B) NWs have larger surface area, pore volume and higher pore size distribution compared with pristine $\text{H}_2\text{Ti}_3\text{O}_7$ NWs (SI-4), which endow the $\text{MnO}_2/\text{TiO}_2$ NWs with more electron/ion paths for feasible ion transport and fast redox reaction.

The as-prepared $\text{MnO}_2/\text{TiO}_2$, $\text{MnO}_2/\text{H}_2\text{Ti}_3\text{O}_7$ NWs and AG materials can be used as freestanding electrodes for assembling asymmetric and symmetric supercapacitor cells. CV and GCD measurements were firstly performed to evaluate the electrochemical potential windows and quantify the specific capacitances of these electrodes in a $1 \text{ M Na}_2\text{SO}_4$ aqueous electrolyte using a three electrode system. The AG was measured within a potential window of -1 to 0 V . The relatively rectangular shape of CV curve (see Supplementary information, SI-8a) is mirror-symmetric with good reversibility, indicating excellent double-layer capacitive behavior for AG electrode. Additionally, the AG electrode exhibits a specific capacitance of 106 F g^{-1} at the current density of 0.5 A g^{-1} in the potential range of -1 to 0 V (see Supplementary information, SI-8b). Therefore, the optimal positive/negative mass ratio of $\text{MnO}_2/\text{TiO}_2$ and AG was set almost 1.50 and $\text{MnO}_2/\text{H}_2\text{Ti}_3\text{O}_7$ and AG was set almost 3.44 based on the balance of the charges (Q).

Based on the above electrochemical characteristics investigation of the individual capacitor, it is possible to combine $\text{MnO}_2/\text{TiO}_2$ or $\text{MnO}_2/\text{H}_2\text{Ti}_3\text{O}_7$ NWs (positive electrode) and AG (negative electrode) to obtain an asymmetric capacitor with a potential window close to 1.8 V. Fig. 9a and b exhibits CV curves of the $\text{MnO}_2/\text{TiO}_2//\text{AG}$ and $\text{MnO}_2/\text{H}_2\text{Ti}_3\text{O}_7//\text{AG}$ asymmetric supercapacitor cell at different potential windows in 1 M Na_2SO_4 aqueous solution at 60 mV s⁻¹. The fabricated asymmetric supercapacitor presents an ideal capacitive behavior with rectangular CV curve. At a potential window of 2.0 V, the CV curve shows a distortion and a slight hump around 2.0 V. This indicates that some irreversible reactions happen when the potential window is higher than 1.8 V [52]. Thus, the optimum working potential window for this asymmetric supercapacitor is from 0 to 1.8 V. Fig. 9b, e exhibits the variation of the specific capacitance with the increase of potential window for the asymmetric supercapacitor. The CV profile of the asymmetric cell remains relatively rectangular at a high scan rate of 80 mV s⁻¹, demonstrating good charge/discharge properties and rate capability of the asymmetric supercapacitor [33]. As shown in Fig. 9c, f the potential of the charge–discharge lines are

nearly proportional to the charge or discharge time, a small equivalent series resistance and an ideal capacitive characteristic, as further confirmed by the EIS date (Fig. 9i). The gravimetric capacitance of the $\text{MnO}_2/\text{TiO}_2//\text{AG}$ and $\text{MnO}_2/\text{H}_2\text{Ti}_3\text{O}_7//\text{AG}$ asymmetric supercapacitor are calculated to be 66.1 and 32 F g⁻¹ based on the total weight of the electrodes, respectively.

To further illustrate the energy and power property of this asymmetric supercapacitor, a Ragone plot is shown in Fig. 9g. In comparison to the $\text{MnO}_2/\text{H}_2\text{Ti}_3\text{O}_7//\text{AG}$ asymmetric supercapacitor, the energy densities of the $\text{MnO}_2/\text{TiO}_2//\text{AG}$ asymmetric supercapacitor are dramatically higher, especially in cases with lower power densities. A maximum energy density of 29.8 Wh kg⁻¹ is obtained for the $\text{MnO}_2/\text{TiO}_2//\text{AG}$ asymmetric supercapacitor, which is more than twice that of the $\text{MnO}_2/\text{H}_2\text{Ti}_3\text{O}_7//\text{AG}$ asymmetric supercapacitor (13.6 Wh kg⁻¹). This result shows an improved energy density compared with a $\text{MnO}_2/\text{SiO}_2//\text{MnO}_2/\text{SiO}_2$ symmetric device (3.75 Wh kg⁻¹) [53], a CNT/ $\text{MnO}_2/\text{GR}/\text{CNT}/\text{PANI}$ asymmetric device (24.8 Wh kg⁻¹) [6], and a $\text{MnO}_2/\text{carbon nanofiber}/\text{active}$

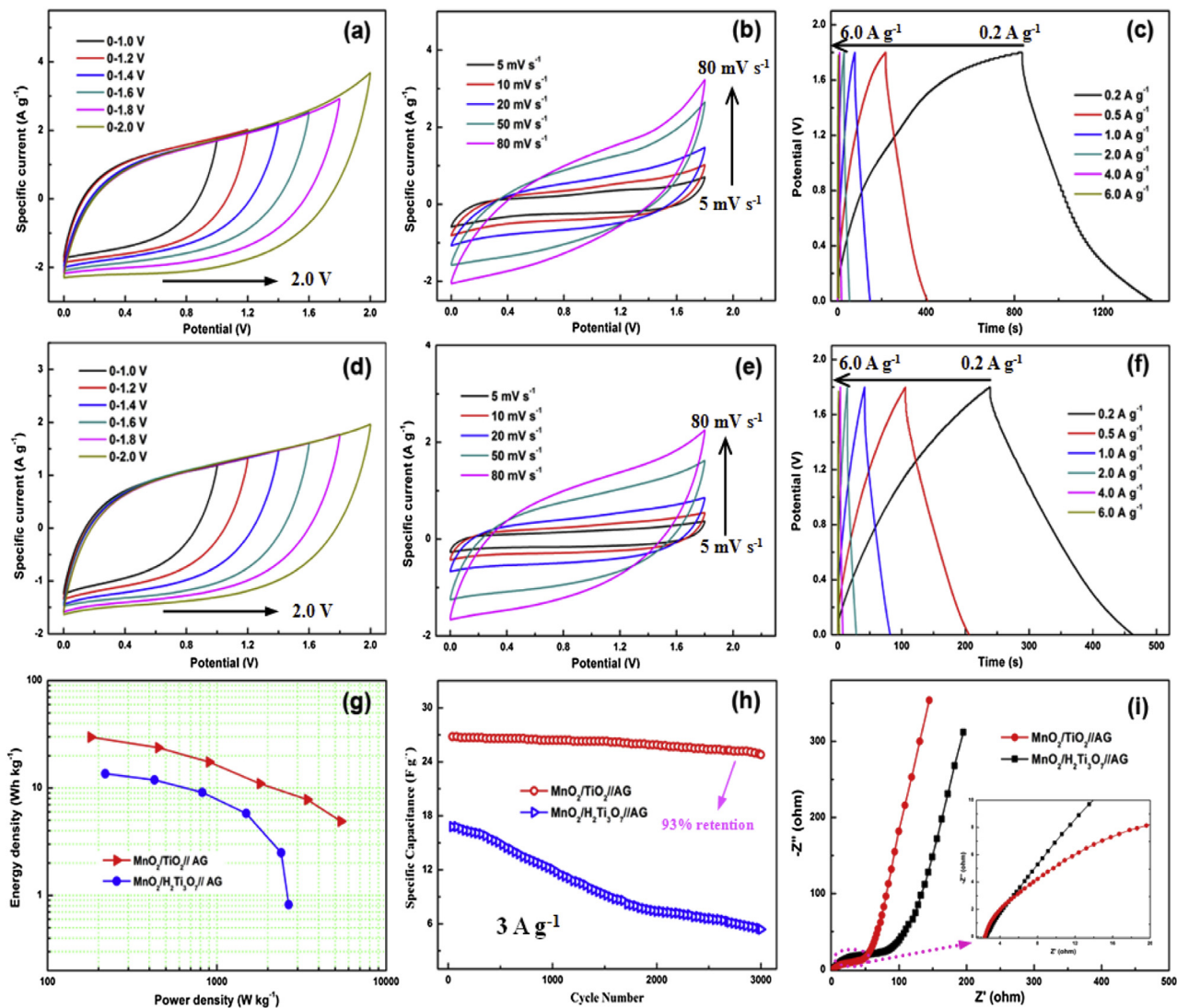


Fig. 9. (a, d) CV curves of the $\text{MnO}_2/\text{TiO}_2//\text{AG}$ and $\text{MnO}_2/\text{H}_2\text{Ti}_3\text{O}_7//\text{AG}$ asymmetric supercapacitor cell measured at different potential windows in 1 M Na_2SO_4 electrolyte, respectively; (b, e) CV curves of the $\text{MnO}_2/\text{TiO}_2//\text{AG}$ and $\text{MnO}_2/\text{H}_2\text{Ti}_3\text{O}_7//\text{AG}$ asymmetric supercapacitor cell measured at different scan rates, respectively; (c, f) charge–discharge curves of the $\text{MnO}_2/\text{TiO}_2//\text{AG}$ and $\text{MnO}_2/\text{H}_2\text{Ti}_3\text{O}_7//\text{AG}$ asymmetric supercapacitor, respectively; (g) Ragone plot of the $\text{MnO}_2/\text{TiO}_2//\text{AG}$ and $\text{MnO}_2/\text{H}_2\text{Ti}_3\text{O}_7//\text{AG}$ asymmetric supercapacitor at the frequencies ranging from 100 kHz to 0.1 Hz. The inset shows the enlarged high frequency range; (h) cycling performance of $\text{MnO}_2/\text{TiO}_2//\text{AG}$ and $\text{MnO}_2/\text{H}_2\text{Ti}_3\text{O}_7//\text{AG}$ asymmetric supercapacitor for charging and discharging at a current density of 3 A g⁻¹; (i) Nyquist plot of the $\text{MnO}_2/\text{TiO}_2//\text{AG}$ and $\text{MnO}_2/\text{H}_2\text{Ti}_3\text{O}_7//\text{AG}$ asymmetric supercapacitor.

carbon nanofiber asymmetric device (8.2 Wh kg^{-1}) [25]. In addition, the specific capacitance, power density, and energy density of the asymmetric supercapacitor at different current densities are also listed in Table S4.

Long cycling life is an important requirement for supercapacitors. The cycling life test over 3000 cycles for the $\text{MnO}_2/\text{TiO}_2/\text{AG}$ and $\text{MnO}_2/\text{H}_2\text{Ti}_3\text{O}_7/\text{AG}$ asymmetric supercapacitor is carried out by repeating the GCD test between 0 and 1.8 V at a current density of 3 A g^{-1} for 3000 cycles (Fig. 9h). The specific capacitance of $\text{MnO}_2/\text{H}_2\text{Ti}_3\text{O}_7/\text{AG}$ asymmetric supercapacitor decreases gradually with increasing cycle numbers and its capacitance retention is only 33% after 3000 cycles. By contrast, $\text{MnO}_2/\text{TiO}_2/\text{AG}$ asymmetric supercapacitor only a little fading can be observed and the capacitance retention is 93% after 3000 cycles.

As previously shown, the $\text{MnO}_2/\text{TiO}_2/\text{AG}$ asymmetric supercapacitor introduces the advantages of the synergism between the two metal-oxides nanomaterials, and these results highlight the capability of the $\text{MnO}_2/\text{TiO}_2/\text{AG}$ asymmetric supercapacitor to meet the requirements of both high specific capacitance and excellent stability, which are important merits for practical energy storage devices.

4. Conclusion

In conclusion, we have prepared ultrathin MnO_2 nanoflakes on $\text{H}_2\text{Ti}_3\text{O}_7$ and TiO_2 NWs via a facile hydrothermal route. Each $\text{H}_2\text{Ti}_3\text{O}_7$ or TiO_2 NWs renders direct contact with the MnO_2 and creates unique supercapacitor electrodes. In view of the difference of surface area and pore volume, the two nanostructures present different pseudocapacitive performance. Electrochemical measurements reveal that the $\text{MnO}_2/\text{TiO}_2$ NWs exhibits much higher specific capacitance and better rate capability compared with $\text{MnO}_2/\text{H}_2\text{Ti}_3\text{O}_7$ NWs. This is because the TiO_2 NWs not only provide high surface area for the deposition of MnO_2 nanoflakes but also improve the electrical conductivity. Therefore, the rational design of $\text{MnO}_2/\text{TiO}_2$ NWs can be used for large-scale fabrication of other promising supercapacitors as well as other power source systems.

Acknowledgments

The authors gratefully acknowledge the financial supports provided by National Natural Science Foundation of China (Grant no. 51104194 and 21103127), Doctoral Fund of Ministry of Education of China (20110191120014), No. 43 Scientific Research Foundation for the Returned Overseas Chinese Scholars, National Key Laboratory of Fundamental Science of Micro/Nano-device and System Technology (2013MS06, Chongqing University), State Education Ministry and Fundamental Research Funds for the Central Universities (Project no. 106112013CDJZR120017 and CDJZR13130035, Chongqing University, PR China). The authors acknowledge support on electrochemical characterization by Dr. Kexin Yao in King Abdullah University of Science and Technology, Saudi Arabia.

Appendix A. Supplementary data

Supplementary data related to this article can be found at <http://dx.doi.org/10.1016/j.jpowsour.2014.07.114>.

References

- [1] D. Bhattacharya, M.-S. Kim, T.-S. Bae, J.-S. Yu, *J. Power Sources* 244 (2013) 799–805.
- [2] L. Huang, D. Chen, Y. Ding, S. Feng, Z.L. Wang, M. Liu, *Nano Lett.* (2013) 3135–3139.
- [3] H. Jiang, C. Li, T. Sun, J. Ma, *Chem. Commun.* 48 (2012) 2606–2608.
- [4] J. Jiang, Y. Li, J. Liu, X. Huang, C. Yuan, X.W. Lou, *Adv. Mater.* 24 (2012) 5166–5180.
- [5] L. Jiang, R. Zou, W. Li, J. Sun, X. Hu, Y. Xue, G. He, J. Hu, *J. Mater. Chem. A* 1 (2013) 478–481.
- [6] Y. Jin, H. Chen, M. Chen, N. Liu, Q. Li, *ACS Appl. Mater. Interfaces* 5 (2013) 3408–3416.
- [7] M. Kim, Y. Hwang, J. Kim, *J. Power Sources* 239 (2013) 225–233.
- [8] L. Zhao, L.Z. Fan, M.Q. Zhou, H. Guan, S. Qiao, M. Antonietti, M.M. Titirici, *Adv. Mater.* 22 (2010) 5202–5206.
- [9] J.-H. Zhong, A.-L. Wang, G.-R. Li, J.-W. Wang, Y.-N. Ou, Y.-X. Tong, *J. Mater. Chem.* 22 (2012) 5656–5665.
- [10] L. Yu, G. Zhang, C. Yuan, X.W. Lou, *Chem. Commun.* 49 (2013) 137–139.
- [11] H. Pang, Y. Ma, G. Li, J. Chen, J. Zhang, H. Zheng, W. Du, *Dalton Trans.* 41 (2012) 13284–13291.
- [12] Z.P. Diao, Y.X. Zhang, X.D. Hao, Z.Q. Wen, *Ceram. Int.* 40 (2014) 2115–2120.
- [13] H. Wang, X. Wang, *ACS Appl. Mater. Interfaces* 5 (2013) 6255–6260.
- [14] L.Z. Fan, Y.S. Hu, J. Maier, P. Adelhelm, B. Smarsly, M. Antonietti, *Adv. Funct. Mater.* 17 (2007) 3083–3087.
- [15] J.S. Shaikh, R.C. Pawar, A.V. Moholkar, J.H. Kim, P.S. Patil, *Appl. Surf. Sci.* 257 (2011) 4389–4397.
- [16] J. Liu, J. Jiang, M. Bosman, H.J. Fan, *J. Mater. Chem.* 22 (2012) 2419.
- [17] J. Liu, C. Liu, Y. Wan, W. Liu, Z. Ma, S. Ji, J. Wang, Y. Zhou, P. Hodgson, Y. Li, *CrystEngComm* 15 (2013) 1578–1585.
- [18] M.V.K. Azhagan, M.V. Vaishampayan, M.V. Shelke, *J. Mater. Chem. A* 2 (2014) 2152–2159.
- [19] W. Zilong, Z. Zhu, J. Qiu, S. Yang, *J. Mater. Chem. C* 2 (2014) 1331–1336.
- [20] X. Xie, C. Zhang, M.B. Wu, Y. Tao, W. Lv, Q.H. Yang, *Chem. Commun.* 49 (2013) 11092–11094.
- [21] R. Ranjusha, K.M. Sajesh, S. Roshny, V. Lakshmi, P. Anjali, T.S. Sonia, A. Sreekumaran Nair, K.R.V. Subramanian, S.V. Nair, K.P. Chennazhi, A. Balakrishnan, *Microporous Mesoporous Mater.* 186 (2014) 30–36.
- [22] S. Wu, W. Chen, L. Yan, *J. Mater. Chem. A* 2 (2014) 2765–2772.
- [23] J.-G. Wang, Y. Yang, Z.-H. Huang, F. Kang, *Electrochim. Acta* 56 (2011) 9240–9247.
- [24] Y. Li, Q. Zhang, J. Zhu, X.-L. Wei, P.K. Shen, *J. Mater. Chem. A* 2 (2014) 3163.
- [25] J.-G. Wang, Y. Yang, Z.-H. Huang, F. Kang, *Carbon* 61 (2013) 190–199.
- [26] P. Roy, R. Berger, P. Schmuki, *Angew. Chem. Int. Ed.* 50 (2011) 2904–2939.
- [27] S. Liu, Z. Wang, C. Yu, H.B. Wu, G. Wang, Q. Dong, J. Qiu, A. Eychmuller, X.W. David Lou, *Adv. Mater.* 25 (2013) 3462–3467.
- [28] X. Lu, M. Yu, G. Wang, T. Zhai, S. Xie, Y. Ling, Y. Tong, Y. Li, *Adv. Mater.* 25 (2013) 267–272.
- [29] J. Wang, Y. Zhou, Z. Shao, *Electrochim. Acta* 97 (2013) 386–392.
- [30] R.B. Ambade, S.B. Ambade, N.K. Shrestha, Y.C. Nah, S.H. Han, W. Lee, S.H. Lee, *Chem. Commun.* 49 (2013) 2308–2310.
- [31] H. He, Y. Zhang, P. Xiao, Y. Yang, Q. Lou, F. Yang, *Bull. Korean Chem. Soc.* 33 (2012) 1613–1616.
- [32] Z. Weng, H. Guo, X. Liu, S. Wu, K.W.K. Yeung, P.K. Chu, *RSC Adv.* 3 (2013) 24758–24775.
- [33] C. Xiang, M. Li, M. Zhi, A. Manivannan, N. Wu, *J. Mater. Chem.* 22 (2012) 19161–19167.
- [34] J. Li, W. Zhao, F. Huang, A. Manivannan, N. Wu, *Nanoscale* 3 (2011) 5103–5109.
- [35] Y. Liu, D. Yan, R. Zhuo, S. Li, Z. Wu, J. Wang, P. Ren, P. Yan, Z. Geng, *J. Power Sources* 242 (2013) 78–85.
- [36] G. Wang, Q. Tang, H. Bao, X. Li, G. Wang, *J. Power Sources* 241 (2013) 231–238.
- [37] Z. Zhang, H. Che, Y. Wang, L. Song, Z. Zhong, F. Su, *Catal. Sci. Technol.* 2 (2012) 1953–1960.
- [38] G. Zhang, W. Li, K. Xie, F. Yu, H. Huang, *Adv. Funct. Mater.* 23 (2013) 3675–3681.
- [39] H. Chen, J. Jiang, L. Zhang, H. Wan, T. Qi, D. Xia, *Nanoscale* 5 (2013) 8879–8883.
- [40] H. Jiang, J. Ma, C. Li, *J. Mater. Chem.* 22 (2012) 16939–16942.
- [41] X. Liu, S. Shi, Q. Xiong, L. Li, Y. Zhang, H. Tang, C. Gu, X. Wang, J. Tu, *ACS Appl. Mater. Interfaces* 5 (2013) 8790–8795.
- [42] X. Li, S. Xiong, J. Li, J. Bai, Y. Qian, *J. Mater. Chem.* 22 (2012) 14276–14283.
- [43] H.-Q. Wang, Z.-S. Li, Y.-G. Huang, Q.-Y. Li, X.-Y. Wang, *J. Mater. Chem.* 20 (2010) 3883–3889.
- [44] T. Zhai, F. Wang, M. Yu, S. Xie, C. Liang, C. Li, F. Xiao, R. Tang, Q. Wu, X. Lu, Y. Tong, *Nanoscale* 5 (2013) 6790–6796.
- [45] A. Ramadoss, S.J. Kim, *Carbon* 63 (2013) 434–445.
- [46] M. Liu, L. Gan, W. Xiong, Z. Xu, D. Zhu, L. Chen, *J. Mater. Chem. A* 2 (2014) 2555–2562.
- [47] M. Kim, Y. Hwang, J. Kim, *J. Mater. Sci.* 48 (2013) 7652–7663.
- [48] J.-X. Feng, Q. Li, X.-F. Lu, Y.-X. Tong, G.-R. Li, *J. Mater. Chem. A* 2 (2014) 2985–2992.
- [49] Y. Luo, D. Kong, J. Luo, S. Chen, D. Zhang, K. Qiu, X. Qi, H. Zhang, C.M. Li, T. Yu, *RSC Adv.* 3 (2013) 14413–14422.
- [50] S. Park, I. Nam, G.P. Kim, J.W. Han, J. Yi, *ACS Appl. Mater. Interfaces* 5 (2013) 9908–9912.
- [51] L. Peng, X. Peng, B. Liu, C. Wu, Y. Xie, G. Yu, *Nano Lett.* 13 (2013) 2151–2157.
- [52] Z. Fan, J. Yan, T. Wei, L. Zhi, G. Ning, T. Li, F. Wei, *Adv. Funct. Mater.* 21 (2011) 2366–2375.
- [53] Y.X. Zhang, M. Huang, F. Li, X.L. Wang, Z.Q. Wen, *J. Power Sources* 246 (2014) 449–456.